Asian Journal of Pharmaceutical Sciences 21 (2026) 101124

Available online at www.sciencedirect.com

ScienceDirect

journal homepage: www.elsevier.com/locate/AJPS



Research Article

Carrier-free reduction-responsive self-assembling paclitaxel dimer nanoprodrug synergizing with celastrol for enhanced chemoimmunotherapy

Yudi Lu[a,#], *Mei Zhou*[a,#], *Xunfa Zhang*[a,#], *Weijun Huang*[a], *Fan Li*[a], *Ning Li Zhang*[a], *Nannan Lu*[a], *Chenggui Wu*[a], *Zhihui Feng*[a,*], *Shuangying Gui*[a,b,c,*], *Zhenbao Li*[a,b,c,d,e,f,*]

[a] *College of Pharmacy, Anhui University of Chinese Medicine, Hefei 230012, China*
[b] *Institute of Pharmaceutics, Anhui Academy of Chinese Medicine, Hefei 230012, China*
[c] *Anhui Province Key Laboratory of Pharmaceutical Preparation Technology and Application, Anhui University of Chinese Medicine, Hefei 230012, China*
[d] *Anhui Province Key Laboratory of the Application and Transformation of Traditional Chinese Medicine in the Prevention and Treatment of Major Pulmonary Diseases, Anhui University of Chinese Medicine, Hefei 230031, China*
[e] *Anhui Provincial Key Laboratory of Tumor Evolution and Intelligent Diagnosis and Treatment, Bengbu Medical University, Bengbu 233030, China*
[f] *Key Laboratory of Xin'an Medicine, Ministry of Education, Anhui University of Chinese Medicine, Hefei 230038, China*

ARTICLE INFO

Article history:
Received 23 August 2025
Revised 3 November 2025
Accepted 24 December 2025
Available online 20 January 2026

Keywords:
Carrier-free
Reduction-responsive
self-assembling
Paclitaxel dimer
Nanoprodrug
Celastrol
Chemoimmunotherapy

ABSTRACT

Chemotherapeutic paclitaxel (PTX) formulations are widely used in clinical cancer treatment; however, they are also associated with concomitant programmed death-ligand (PD-L1) upregulation and an immunosuppressive microenvironment. Herein, we rationally designed carrier-free, reduction-sensitive PTX dimer self-assembling nanoprodrugs (diPC NPs), composed of a glutathione (GSH)-responsive PTX dimer prodrug (diPTX) and the PD-L1 downregulator celastrol (Cel) for combinational chemoimmunotherapy. Following intravenous administration, the diPC NPs exhibited prolonged blood circulation and preferential tumor accumulation by exploiting the enhanced permeability and retention effect. Subsequently, the elevated GSH levels in tumor cells cleaved the disulfide bonds, triggering the rapid release of PTX and Cel. The released PTX elicited potent cytotoxic effects and induced immunogenic cell death (ICD), whereas the released Cel synergistically enhanced ICD and downregulated PD-L1 expression in tumor cells. Together, these effects resulted in remarkable antitumor efficacy with exhibited a favorable safety profile within the therapeutic window in both Lewis lung carcinoma cells and B16F10 tumor-

* Corresponding authors.
E-mail addresses: fzh@ahtcm.edu.cn (Z. Feng), guishy0520@126.com (S. Gui), lizhenbao@ahtcm.edu.cn (Z. Li).
# These authors contributed equally to this work.
Peer review under responsibility of Shenyang Pharmaceutical University.

https://doi.org/10.1016/j.ajps.2026.101124
1818-0876/© 2026 Shenyang Pharmaceutical University. Published by Elsevier B.V. This is an open access article under the CC BY-NC-ND license (http://creativecommons.org/licenses/by-nc-nd/4.0/)

bearing mice. Our findings highlight a promising strategy for highly efficient combination chemoimmunotherapy.

© 2026 Shenyang Pharmaceutical University. Published by Elsevier B.V.
This is an open access article under the CC BY-NC-ND license
(http://creativecommons.org/licenses/by-nc-nd/4.0/)

1. Introduction

Given the rising global incidence of cancer and the persistent challenges in its treatment, oncology research has become a critical priority in modern medicine [1,2]. Chemotherapy remains a cornerstone in cancer management [3]. Among chemotherapeutic agents, paclitaxel (PTX) is widely employed as a first-line treatment for various solid tumors, including lung, breast and ovarian cancers [4]. Its primary mechanism involves binding to cellular microtubules, arresting the cell cycle, and inducing tumor cell apoptosis, thereby inhibiting tumor progression [5,6]. Beyond its direct cytotoxicity, PTX can also induce immunogenic cell death (ICD), a process characterized by the release of tumor-associated antigens and damage-associated molecular patterns (DAMPs) [7]. These signals promote dendritic cell (DC) maturation and subsequent T cell activation, ultimately enhancing the immunosuppressive tumor microenvironment (TME) [8]. However, PTX treatment simultaneously upregulates programmed death-ligand 1 (PD-L1) expression on tumor cells, thereby activating immune evasion through the programmed cell death protein 1 (PD-1)/PD-L1 checkpoint axis and ultimately compromising therapeutic efficacy [9]. Consequently, PTX-based chemotherapy often requires combination with PD-L1 inhibitors to elicit maximal antitumor immune responses [10].

As a major breakthrough in cancer immunotherapy, PD-1/PD-L1 blockade therapy has demonstrated clinical efficacy across a range of solid tumors, significantly improving treatment outcomes. Nevertheless, limited response rates and severe immune-related adverse effects restrict the broader clinical application of PD-1 or PD-L1 antibodies [11–13]. Traditional Chinese medicine (TCM) represents a valuable source for anticancer drug discovery [14,15]. Natural compounds derived from TCM exhibit promising therapeutic potential, demonstrating enhanced efficacy and reduced toxicity compared with conventional chemotherapeutics [16]. Celastrol (Cel), a pentacyclic triterpenoid isolated from *Tripterygium wilfordii*, possesses broad-spectrum antitumor activity [17]. It not only induces autophagy and triggers ICD—facilitating DAMP release, DC activation and TME modulation, but also downregulates PD-L1 expression on tumor cells, thereby suppressing immune evasion, and enhancing antitumor immunity [18,19]. Both PTX and Cel directly kill tumor cells, activate multiple signaling pathways and systemic immune responses, and inhibit tumor growth and metastasis. However, their poor solubility and nonspecific biodistribution present major obstacles to developing effective combination formulations [20,21].

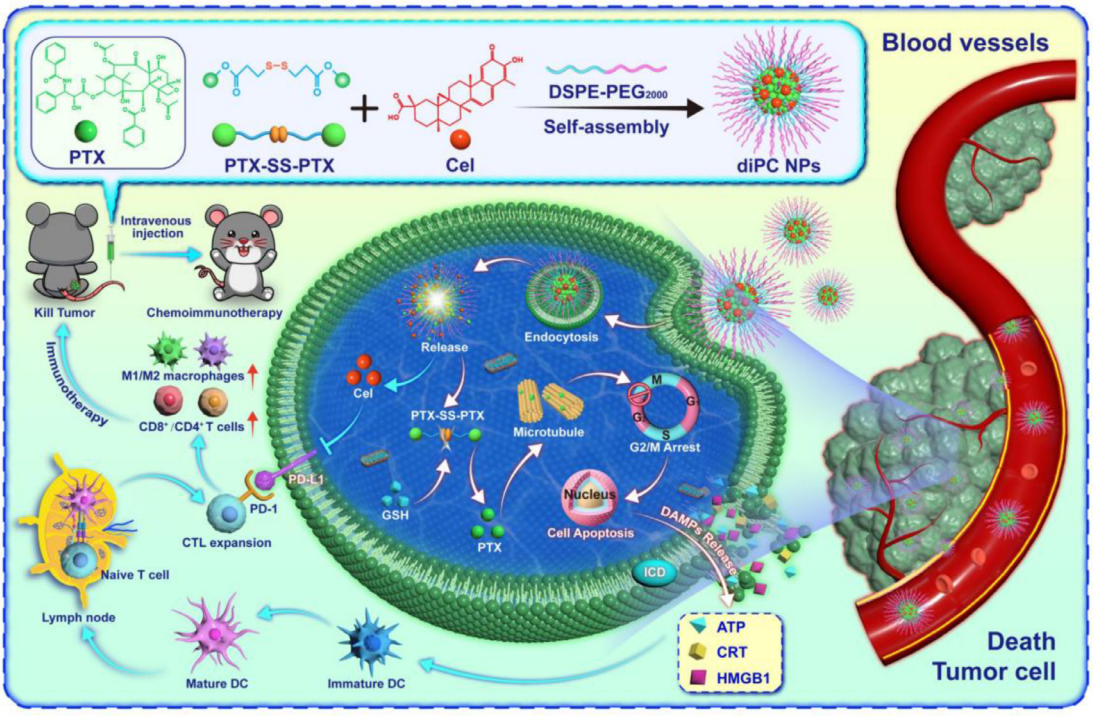
The integration of prodrug strategies with nanotechnology has greatly advanced nanoparticle-based combination tumor therapy. Prodrug design enhances pharmacokinetic properties by improving solubility and metabolic stability [22], whereas nanocarriers leverage the EPR effect to achieve tumor-selective accumulation and on-demand drug release [23,24]. In our previous studies, we notably found that small-molecule hydrophobic prodrugs could self-assemble into uniform nanoassemblies *via* a simple one-step nanoprecipitation method. Using this approach, we developed a series of stimuli-responsive nanoprodrugs, including redox-labile dimeric PTX NPs, disulfide-bridged PTX-16-methylheptadecanoic acid prodrug nanoassemblies, carbon-spaced tandem-disulfide-linked PTX nanoprodrugs, hybrid sulphur bond-linked DTX-STeS-DTX NPs, and reactive oxygen species-responsive PTX–pyropheophorbide a dimers for efficient tumor therapy [25–31]. In tumor-bearing mouse models, these newly fabricated nanoprodrugs demonstrated exceptionally high drug loading, excellent colloidal stability, prolonged circulation, enhanced tumor accumulation, tumor-selective activation, and superior antitumor efficiency with negligible toxicity upon intravenous administration. Similar to commercial PTX formulations, however, these PTX-based nanoprodrugs also upregulated PD-L1 expression and promoted an immunosuppressive microenvironment.

In this study, we rationally engineered carrier-free self-assembling prodrug nanoparticles (diPC NPs) comprising a glutathione (GSH)-responsive PTX dimer prodrug (diPTX) and Cel for synergistic chemoimmunotherapy. The diPC NPs were fabricated through a one-step nanoprecipitation method using DSPE-PEG_{2000} as a stabilizer. After intravenous injection, the NPs exhibited prolonged systemic circulation and enhanced tumor accumulation *via* the passive EPR effect. Once internalized by tumor cells, intracellular GSH cleaved the disulfide bonds within diPTX, resulting in the rapid release of PTX and Cel. The released PTX induced apoptosis and ICD, characterized by CRT exposure, high-mobility group box 1 protein (HMGB1) secretion, and adenosine triphosphate (ATP) efflux, while the released Cel downregulated PTX-induced PD-L1 expression and remodeled the tumor immune microenvironment by recruiting recruit cytotoxic T lymphocytes and repolarizing macrophages. This synergistic interaction achieved potent antitumor efficacy with minimal systemic toxicity (Scheme 1). Overall, this study presents a rational strategy combining an ICD inducer with a PD-L1 downregulator for highly efficient, low-toxicity synergistic chemoimmunotherapy.

2. Materials and methods

2.1. Materials

PTX (98%) was purchased from Nanjing Jingzhu Biotechnology Co., Ltd. (Nanjing, China). 3,3′-dithiodipropionic acid (98%)



Scheme 1 – Schematic illustration of the formulation of carrier-free, reduction-responsive self-assembling diPC NPs and their synergistic chemoimmunotherapy with minimal toxicity after intravenous injection.

was obtained from Energy Chemical (Shanghai, China). 1-ethyl-3-(3-dimethylaminopropyl)carbodiimide hydrochloride was purchased from Shanghai Macklin Biochemical Co., Ltd. (Shanghai, China) (98%). 4-dimethylaminopyridine (98%) was purchased from Shanghai Aladdin Biochemical Technology Co., Ltd. (Shanghai, China). Cel (98%) was sourced from Macklin Biochemical Technology Co., Ltd. (Shanghai, China). DSPE-PEG_{2000} was acquired from Xi'an Ruixi Biological Technology Co., Ltd. (Xian, China). Coumarin 6 (C-6), 1,1′-dioctadecyl-3,3,3′,3′-tetramethylindotricarbocyanine iodide (DiR), dithiothreitol (DTT), the Cell Counting Kit-8 (CCK-8) assay kit, the enhanced ATP assay kit and Horseradish peroxidase (HRP)-conjugated goat anti-rabbit IgG were from Beyotime Biotechnology Co., Ltd. (Shanghai, China). 4′,6-Diamidino-2-phenylindole (DAPI) was purchased from Wuhan Servicebio Technology Co., Ltd. (Wuhan, China). The HMGB1 ELISA kit was procured from Shanghai Jianglai Biotechnology Co., Ltd. (Shanghai, China). Alexa Fluor 647-anti-calreticulin antibody was purchased from Novus Biologicals (Missouri, USA). PE-anti-CD274 antibody was supplied by eBioscience (San Diego, CA, USA). The PE/Dazzle^{TM} 594-anti-CD3, Brilliant Violet 510^{TM}-anti-CD4, PerCP-Cy5.5-anti-CD8, Brilliant Violet 421^{TM}-anti-F4/80, APC-anti-CD80, and PE-anti-CD206 antibodies were obtained from BioLegend (San Diego, CA, USA). PD-L1 and GAPDH primary antibodies were purchased from Abcam (Cambridge, UK).

Sprague-Dawley (SD) rats and C57BL/6 mice were purchased from Henan Skobes Biotechnology Co., Ltd. (Anyang, China). All animal experiments were approved by the Animal Care and Use Committee of Anhui University of Chinese Medicine.

2.2. *Preparation and characterization of diPC NPs*

The diPC NPs were fabricated using a one-step nanoprecipitation approach. Briefly, diPTX, Cel and DSPE-PEG_{2000} at a 5:1:2 (w/w/w) ratio were co-dissolved in 1 mL of a blended solvent system (ethanol:tetrahydrofuran = 7:1, v/v). Under vigorous stirring, the resulting mixture was introduced dropwise into 5 ml deionized water. Following this, organic solvents were eliminated *via* rotary evaporation, yielding the final diPC NP product.

For physicochemical characterization, the NPs suspension was diluted 10-fold with deionized water. The hydrodynamic diameter and zeta potential were measured using a Malvern Zetasizer (Malvern, USA) analyzer. For morphological examination, the nanoparticle suspension was diluted, applied to carbon-coated copper grids, and blotted to remove excess solution. Following air-drying, the samples were negatively stained with 2% phosphotungstic acid and examined using transmission electron microscopy (TEM) (JEOL-2010, JEOL, Japan).

2.3. *Stability evaluation of diPC NPs*

The freshly prepared NPs (1 ml) were mixed with 9 ml phosphate-buffered saline (PBS) (pH 7.4) containing 10% fetal bovine serum (FBS) to simulate physiological conditions. The mixture was incubated at 37 °C under gentle agitation (100 rpm), and the particle size was monitored at predetermined time intervals (0, 2, 4, 6, 8, 12 and 24 h). For long-term stability assessment, the NPs suspension was diluted 10-fold with deionized water and stored at 4 °C. The

hydrodynamic diameter was periodically measured (on Day 1, 2, 3, 4, 5, 6, 7, 11, 14, 20 and 33) to evaluate storage stability.

2.4. Self-assembly mechanism of diPC NPs

The prepared nano-formulation (1 ml) was uniformly mixed with 9 ml deionized water, sodium chloride (NaCl) solution, urea solution or Triton X-100 solution, respectively. After incubation at room temperature for 12 h, the particle size changes of the NPs were measured.

2.5. In vitro release study of diPC NPs

An aliquot of NP suspension (equivalent to 200 μg PTX) was added to 30 ml PBS (pH 7.4) containing 30% (v/v) anhydrous ethanol, with or without 10 mM DTT. The entire system was placed in a constant-temperature shaker set at 37 °C and 100 rpm. At predetermined time intervals (0, 2, 4, 6, 8, 12, 24 and 48 h), 100 μl samples were withdrawn and analyzed using high-performance liquid chromatography (HPLC) (LC20AD, Shimadzu Corporation, Japan) to determine the concentration of free drug.

2.6. Cell lines and culture

The mouse embryonic fibroblast cell line (3T3), mouse Lewis lung carcinoma cells (LLC), and mouse melanoma cells (B16F10) were acquired from NOBLEBIO Biotechnology Co., Ltd. (Hangzhou, China). The NIH 3T3 (mouse embryonic fibroblast), LLC (mouse lung adenocarcinoma) and B16F10 (mouse melanoma) cell lines were cultured in Dulbecco's Modified Eagle Medium (GIBCO) supplemented with 10% (v/v) FBS (GIBCO). All cells were maintained in a humidified incubator at 37 °C with 5% CO_2, with the culture medium replaced daily.

2.7. Cytotoxicity assay

The cell viability of 3T3, LLC, and B16F10 cells treated with various formulations was evaluated using the CCK-8 assay. The cells in the logarithmic growth phase with good growth status were seeded in 96-well plates at a density of 2×10^3 cells/well and cultured for 24 h at 37 °C with 5% CO_2. After removing the old medium, 100 μl serially diluted formulations (concentrations: 4000, 2000, 1000, 500, 250, 125, 62.5, 31.25 and 15.625 nmol/l) in fresh medium was added to each well. Complete medium without drugs served as the negative control, with six replicate wells per group. Following 48 h of treatment, the medium was aspirated and replaced with 100 μl serum-free medium containing 10% CCK-8 solution. Following a 2-h incubation period at 37 °C, the absorbance of each well was determined at a wavelength of 450 nm using a microplate reader (Ensight, PerkinElmer, USA).

2.8. Cellular uptake investigation

Using C-6 as a fluorescent probe, C-6-labelled C/diPTX, C/diPC, and C/Cel NPs were prepared, respectively, with C-6 solution as control. The cells were seeded in 6-well plates at a density of 4×10^5 cells/well and cultured in a 37 °C, 5% CO_2 incubator for 24 h. After removing the old medium, fresh medium containing diluted C-6 solution or C-6-labelled prodrug self-assembled NPs (final C-6 concentration, 100 ng/ml for all) was added, followed by incubation for 0.25 h and 1 h, respectively. Following incubation, the drug-loaded medium was removed, and ice-cold PBS (pH 7.4) was added to halt cellular internalization. The cells were subsequently subjected to three washes using PBS (pH 7.4) and then detached using 0.25% trypsin. Digestion was stopped by adding fresh complete medium. After centrifugation at 1200 rpm for 5 min, the supernatant was discarded and the cells were collected. The cells were resuspended in 300 μl ice-cold PBS (pH 7.4) and analyzed using flow cytometry (FCM) (BDFACSCelesta, BD Biosciences, USA).

For confocal microscopy observation, the cells were seeded on coverslips in 12-well plates at a density of 1.5×10^5 cells/well and cultured for 24 h. After removing the old medium, serum-free medium containing a C-6 solution or labelled self-assembled NPs (final C-6 concentration, 50 ng/ml for all groups) was added, followed by incubation for 0.25 h and 1 h, respectively. Following incubation, the cells underwent three washes with ice-cold PBS (pH 7.4), fixation in 4% paraformaldehyde for 15 min, and nuclear staining with DAPI for 3 min. Cellular internalization was subsequently visualized using confocal laser scanning microscopy (CLSM) (Zeiss LSM900, Germany).

2.9. Detection of in vitro ICD induction and PD-L1 expression

The cells were plated in 6-well plates at a density of 4×10^5 cells per well and allowed to adhere for 24 h. Afterwards, the spent medium was aspirated and replaced with fresh medium containing the drug formulations (equivalent Cel concentration, 1500 nM). After a 12-h incubation period, the medium containing the drug was aspirated. The cells were then rinsed with PBS, detached using trypsin, and harvested for further analysis. The cells were incubated with Alexa Fluor 647-labelled CRT antibody (1:100, v/v) or PE-labelled PD-L1 antibody (1:100, v/v) at 4 °C in the dark for 30 min. Following resuspension in PBS, CRT exposure and PD-L1 expression were analyzed using FCM.

The cells were plated in 24-well plates at a density of 2×10^4 cells per well and allowed to adhere for 24 h. Afterwards, the spent medium was aspirated and replaced with fresh medium containing the drug formulations (equivalent Cel concentration, 1500 nM). After 12-h incubation, the cells were centrifuged to collect the supernatant. ATP release was detected using an Enhanced ATP Assay Kit, according to the manufacturer's instructions. HMGB1 secretion was detected using the ELISA Kit.

2.10. In vivo pharmacokinetic study

Male SD rats were used as the pharmacokinetic model and randomly divided into four groups ($n = 3$). The pharmacokinetic experiment was conducted when the rats weighed between 180 and 220 g. Prior to the experiment, the rats were fasted and weighed to determine the administration

dose. DiR was selected as the fluorescent label for NPs, and a DiR solution (DiR-Sol) was prepared as the control group. The administration dose was equivalent to 2 mg/kg of DiR. After administration, blood samples were collected from the orbital venous plexus of the SD rats at predetermined time points (0.083, 0.25, 0.5, 1, 2, 4, 8, 12 and 24 h). The blood samples were centrifuged (8000 rpm, 3 min) to obtain plasma supernatant. Subsequently, 50 μl the supernatant was combined with 450 μl methanol in 1.5 mL EP tubes, vigorously vortex-mixed, and centrifuged at 12,000 rpm for 10 min. Following this, 200 μl the clarified supernatant was carefully transferred to black 96-well plates for further analysis. The fluorescence intensity of DiR in different groups was measured using a multifunctional microplate reader (PerkinElmer, USA) (excitation wavelength, 748 nm; emission wavelength, 780 nm).

2.11. *In vivo tissue distribution study*

Female C57BL/6J mice with subcutaneous tumor xenografts were used as the model. LLC or B16F10 cells (2×10^6 cells in 100 μl) were subcutaneously inoculated into the right dorsal flank of the mice. When the tumor volume reached approximately 300 mm^3, the mice were randomly assigned to eight groups. The following formulations were administered *via* tail vein injection at an equivalent DiR dose of 2 mg/kg: DiR-Sol, diPTX/DiR NPs, diPC/DiR NPs, and Cel/DiR NPs. *In vivo* fluorescence imaging was performed at 4 h and 24 h post-injection under anesthesia using a small animal live imaging system (IVIS Spectrum, PerkinElmer, USA). Subsequently, heart, liver, spleen, lungs, kidneys and tumors were harvested from each mouse and placed in the small animal imaging system to observe the accumulation of the photosensitizer in *ex vivo* tissues, followed by quantitative analysis.

2.12. *Evaluation of in vivo antitumor efficacy and safety*

Six-week-old C57BL/6J mice were acclimatized and then subcutaneously inoculated with LLC or B16F10 cells (2×10^6 cells in 100 μl) on the right dorsal flank. When tumor volumes reached approximately 100 mm^3, the mice were randomly divided into seven groups ($n = 5$ per group). On Day 0, the following treatments were administered *via* tail vein injection: saline (control), diPTX NPs, diPC NPs, Cel NPs, Taxol, Taxol&Cel-Sol, and Cel-Sol (all at equivalent doses of 10 mg/kg PTX and 2 mg/kg Cel). The treatments were repeated every 2 d Body weight and tumor volume were measured daily, with tumor volume being calculated using the following standard formula: V = (tumor length) × (tumor width)^2/2. After the treatment, the mice were euthanized by cervical dislocation, and the tumor tissues were extracted for photographic documentation and weighing. Subsequently, part of the tumor was immersed in 4% paraformaldehyde for section staining, such as hematoxylin and eosin (H&E), Kiel 67 (Ki67), and terminal deoxynucleotidyl transferase dUTP nick-end labelling (TUNEL). The eyeballs were enucleated to collect whole blood and serum from the mice for a complete blood count (CBC) and liver/kidney function analysis. Major organs (heart, liver, spleen, lungs, and kidneys) were harvested for H&E staining to evaluate the safety of the NPs. The excised tumors were minced and placed in Roswell Park Memorial Institute-1640 medium containing 0.1% collagenase IV, 0.025% DNase and 10% FBS, followed by digestion at 37 °C for 60 min. The resulting cell suspension was filtered and centrifuged and then blocked on ice with CD16/32 antibody diluted at a 1:100 ratio. Subsequently, diluted antibodies at 1:50 against CD3, CD4, CD8 or F4/80, CD80, or CD206 were added and incubated on ice in the dark for 30 min. After washing with PBS, the samples were analyzed using FCM. Meanwhile, tumor sections were prepared for immunofluorescence staining of CRT, HMGB1 and PD-L1.

2.13. *Western blotting*

In total, 80 mg tumor tissues stored was retrieved at –80 °C and homogenized in 500 μl radioimmunoprecipitation buffer (Beijing Prilosec Gene Technology Co, China) using a pre-chilled mortar and pestle on ice. The homogenate was centrifuged at 12,000 × g for 15 min at 4 °C to pellet the debris. The supernatant was collected. The supernatant was mixed with 5× Laemmli loading buffer (1:4 ratio) and denatured at 95 °C for 5 min. A 10% sodium dodecyl sulphate-polyacrylamide gel was prepared. The samples were loaded and run at 80 V (stacking gel) followed by 120 V (separating gel) until the proteins were adequately resolved. The proteins were transferred to a 0.45-μm polyvinylidene fluoride membrane (Thermo Fisher Scientific, China) at 260 mA for 1 h under cooling at 4 °C. The membrane was blocked with 5% non-fat milk prepared in Tris-Buffered Saline with Tween 20 (TBST) (Thermo Fisher Scientific, China) for 2 h at room temperature. Following blocking, it was incubated overnight at 4 °C with primary antibodies diluted in 5% BSA/TBST. After washing, the membrane was treated with HRP-conjugated secondary antibodies at a dilution of 1:5000 (v/v in TBST) for 1 h at room temperature. The chemiluminescent signals were detected using a chemiluminescence imaging system (Tanon-5200, Tianneng Technology Co, China). Band intensity was quantified using the ImageJ software.

2.14. *Statistical analyses*

Statistical analyses were performed using one-way analysis of variance, with a $P < 0.05$ considered statistically significant. Graphs and curve fitting were generated using GraphPad Prism version 8.0.

3. Results and discussion

3.1. *Preparation, characterization and release of diPC NPs*

Initially, PTX was conjugated with 3,3′-dithiodipropionic acid to synthesize a disulphide-bridged PTX prodrug (diPTX) [32]. The structure of diPTX was confirmed using ^{1}H NMR and mass spectrometry (MS), and its purity was >98%, as verified using HPLC (Fig. S1–S4), meeting the requirements for the subsequent experiments. Using DSPE-PEG2000 as the carrier matrix, diPTX and Cel were co-assembled into diPC NPs using the nanoprecipitation method, with diPTX NPs and Cel

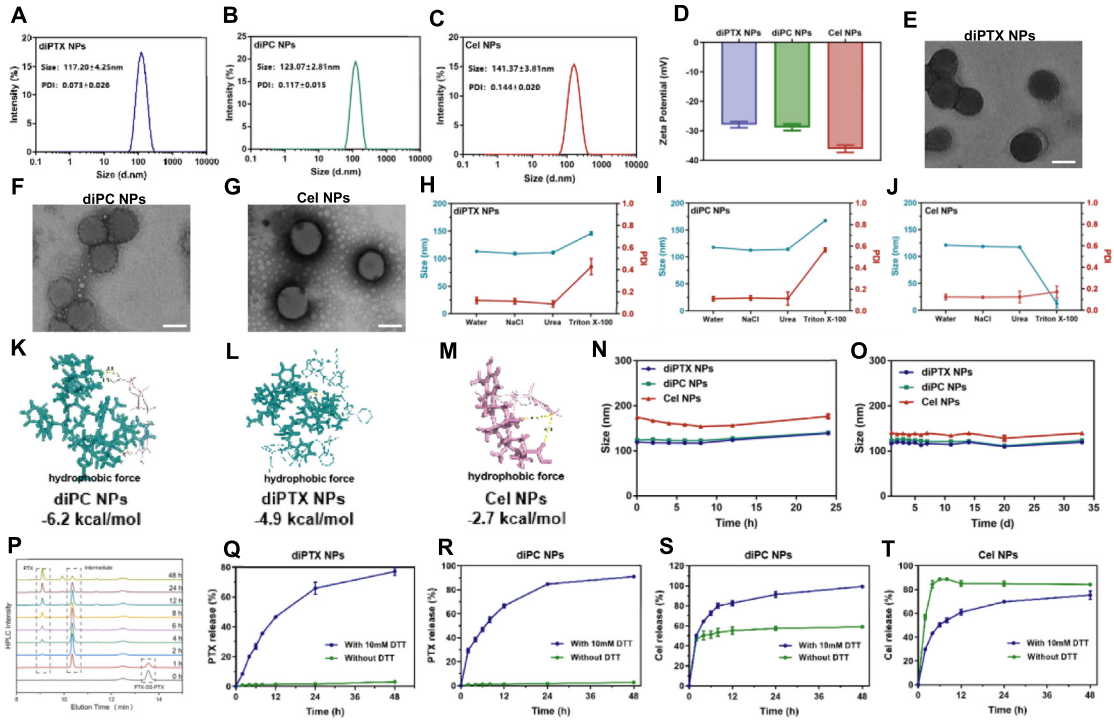


Fig. 1 – Preparation, characterization and *in vitro* release profiles of reduction-responsive nanoprodrugs. The particle size and polydispersity index (PDI) of (A) diPTX, (B) diPC and (C) Cel NPs were determined. Surface charge properties assessed *via* (D) zeta potential. The morphological characteristics of (E) diPTX, (F) diPC, and (G) Cel NPs were assessed using TEM (scale bar: 100 nm). After 24-h treatment with water, NaCl, urea and Triton X-100: Changes in particle size and PDI of (H) diPTX, (I) diPC, and (J) Cel NPs. The molecular docking and binding energy of (K) diPTX, (L) diPC, and (M) Cel NPs. (N) Plasma stability and (O) long-term stability of diPTX, diPC and Cel NPs. Under DTT conditions: (Q) PTX release rate of diPTX NPs; (P) HPLC chromatogram, (R) PTX and (S) Cel release rates of diPC NPs; (T) Cel release rate of Cel NPs. Error bars represent standard deviation (SD, $n = 3$).

NPs prepared as controls. Dynamic light scattering revealed hydrodynamic diameters of 117.20 ± 4.25 nm (diPTX NPs), 123.07 ± 2.81 nm (diPC NPs), and 141.37 ± 3.81 nm (Cel NPs), with zeta potentials of –27.93 ± 1.06 mV, –28.80 ± 1.10 mV, and –36.10 ± 1.21 mV, respectively (Fig. 1A–1D). All three formulations exhibited low polydispersity indices (Table S2), with optimal NP sizes and negative zeta potentials that are favorable for prolonged systemic circulation and enhanced tumor accumulation through the EPR effect. TEM further confirmed the spherical morphology and homogeneity of the NPs (Fig. 1E–1G).

To elucidate the self-assembly mechanism, the NPs were incubated with various media to monitor size variations. Although negligible changes occurred in NaCl or urea solutions compared with deionized water, significant size alterations were observed upon Triton X-100 treatment (Fig. 1H–1J), suggesting hydrophobic interactions as the predominant driving force for NP assembly. Molecular docking simulations quantified the thermodynamic stability of the assemblies, revealing Gibbs free energy changes of –4.9 kcal/mol (diPTX NPs), –6.2 kcal/mol (diPC NPs), and –2.7 kcal/mol (Cel NPs) during drug aggregation processes (Fig. 1K–1M). Among them, under hydrophobic force, the energy released by diPC NPs was the highest, whereas the energy of the self-assembled system was the lowest, indicating superior thermodynamic stability. The plasma stability assays (Fig. 1N) and long-term storage assessments (Fig. 1O) further demonstrated negligible degradation of all three NPs in biofluids and a shelf life of >4 weeks.

The reduction-responsive drug release is a critical determinant of therapeutic efficacy. Therefore, we used 10 mM DTT as the release medium to evaluate the drug release profile by simulating the intracellular reduction-responsive microenvironment. Initial assessment of reduction-responsive sensitivity was performed by monitoring evolution of NP size under reducing conditions. All three NP formulations exhibited time-dependent structural disruption, as demonstrated by the development of polydisperse size distributions (Fig. S5). For diPTX and diPC NPs, the increase in average hydrodynamic diameter was attributed to DTT-mediated cleavage of the disulphide bonds, leading to structural disintegration. However, the observed size variation in Cel NPs likely originated from a Michael addition reaction between DTT and the α, β-unsaturated ketone moiety of A/B rings in Cel (Fig. S6–S7). Subsequently, the drug release profiles of the NPs were quantitatively assessed using HPLC. In the presence of DTT, both diPTX and diPC NPs demonstrated sustained PTX release profiles, achieving

approximately 80% cumulative release over 48 h, whereas diPC NPs achieved complete Cel release (~100%). Cel NPs released ~70% of the Cel payload. In contrast, in DTT-free PBS, diPTX and diPC NPs released only 3% of free drug within 48 h, conclusively confirming their robust reduction-responsive behavior (Fig. 1P–1T). Notably, the addition of DTT to Cel NPs resulted in a reduced release rate of Cel. This phenomenon could be attributed to the formation of an intermediate through the reaction between DTT and Cel, which may retard drug release. The A/B ring of Cel acts as a Michael acceptor, enabling a Michael addition reaction with the thiol groups of thiol-containing compounds, such as DTT. To confirm this reaction, we used HPLC analysis, which revealed a new peak upon addition of DTT. Furthermore, MS was used to characterize the resultant product, indicating a molecular formula of $C_{33}H_{48}O_6S_2$ for the proposed adduct (Fig. S8–S9).

3.2. Cytotoxicity and cellular uptake

The cytotoxic effects of NP formulations (diPTX, diPC, Cel NPs) and corresponding solution controls (Taxol, Taxol&Cel-Sol, Cel-Sol) were evaluated in 3T3, LLC and B16F10 cell lines using the CCK-8 assay. Significantly, our formulation demonstrated selective toxicity toward tumor cells, and attenuated cytotoxicity was observed in normal 3T3 cells compared with tumor cells, which may be attributed to the rapid cleavage of nanoprodrugs in tumor cell but a limited cleavage in 3T3 cell, robustly implying a high tumor-selective capability with preferable selection index of prodrug nanoassemblies. In addition, the diPC NPs exhibited lower IC_{50} values than both diPTX and Cel NPs in LLC and B16F10 cells, demonstrating superior antitumor efficacy. However, the Taxol and Taxol&Cel-Sol solution groups showed significantly stronger cytotoxic effects across all four cell lines compared with diPTX and diPC NPs. This difference may be attributed to the different uptake pathway and release performances of these formulations, where solutions with free diffusion-mediated transcellular pathway presented immediate and complete drug release, whereas internalization-mediated prodrug NPs required a suitable time to trigger drug release to reach therapeutic concentrations (Fig. 2A–2C, Table S3).

We used C-6 as a fluorescent probe to prepare C-6-loaded C/diPTX NPs, C/diPC NPs, and C/Cel NPs and investigated the uptake behavior of each NP group in 3T3, LLC, and B16F10 cells, respectively, by tracking C-6. The results of FCM revealed that NP uptake in all three cell lines was significantly higher than that of the C-6 solution, exhibiting a time-dependent increase. This difference can be attributed to the distinct cellular internalization mechanisms, with NPs entering the cells primarily *via* endocytosis, whereas small molecules in solution passively diffuse. These results further demonstrated that DSPE-PEG_{2000}-modified NPs effectively enhanced drug uptake efficiency (Fig. 2D–2F). CLSM was used to further confirm the high cellular uptake efficiency of the NPs. The results revealed that, after 1 h of incubation, all three NP formulations displayed markedly stronger green fluorescence signals in the cell lines compared with the free drug solution. Additionally, the fluorescence intensity at 1 h surpassed that observed at 0.25 h, demonstrating a time-dependent cellular uptake pattern (Fig. 2G–2I).

3.3. ICD induction and PD-L1 downregulation

ICD plays a critical role in antitumor immunotherapy, and PTX can induce ICD in tumor cells, accompanied by CRT exposure, HMGB1 secretion, and ATP release [28,33,34]. Given the critical role of ICD in antitumor immunity, we examined the ICD activation properties of diPC NPs in LLC and B16F10 cells. Quantitative analysis showed that diPC NPs significantly enhanced CRT exposure (evidenced by a 1.3-fold higher fluorescence intensity *vs.* control), outperforming diPTX and Cel NPs (0.8- and 0.2-fold increase, respectively) in LLC cells (Fig. 3B), while also increasing HMGB1 secretion (Fig. 3D–3E) and ATP efflux (Fig. 3F–3G). These results confirmed that diPC NPs could induce ICD in tumor cells. However, owing to their controlled release properties, the overall ICD-triggering capability of the NPs was slightly inferior to that of the corresponding solution formulations, which was consistent with the consequences of CLSM. Regardless of whether in LLC or B16F10 cells, all treatment groups were able to induce ICD to varying degrees. The diPC NPs group exhibited stronger CRT fluorescence than the diPTX and Cel NPs groups, along with weaker HMGB1 fluorescence, demonstrating a more potent ability to induce ICD. The overall ICD-triggering capability of the NPs was moderately inferior to that of their corresponding solution formulations (Fig. S10).

PTX upregulates PD-L1 expression on tumor cells, thereby attenuating the antitumor immune response *via* the immune checkpoint pathway [35], whereas Cel exhibits PD-L1 downregulating effects and may potentially enhance immunotherapeutic outcomes [36]. To assess the immunomodulatory potential of diPC NPs, we further evaluated the effects of diPC NPs on PD-L1 expression in LLC and B16F10 cells. Notably, although diPTX NPs induced PD-L1 upregulation, diPC and Cel NPs significantly suppressed PD-L1 expression (Fig. 3H–3I). These results demonstrated that the incorporation of Cel into diPC NPs effectively counteracted PTX-mediated elevation of PD-L1, resulting in favorable immunomodulation. This dual-action mechanism positions diPC NPs as a promising candidate for tumor immunotherapy applications.

3.4. Pharmacokinetics and biodistribution

The *in vivo* circulation time of NPs is critical for their passive accumulation within tumors. To evaluate the prolonged circulation conferred by DSPE-PEG_{2000} modification, we performed pharmacokinetic analysis using DiR-labelled NPs. By calculating relevant pharmacokinetic parameters, we found that compared with the DiR solution, self-assembled NPs significantly increased the area under the curve (AUC_{0-24h}) and half-life ($t_{1/2}$), indicating extended circulation (Fig. S11, Table S4). Notably, the AUC_{0-24h} and $T_{1/2}$ of Cel NPs were significantly lower than those of diPTX and diPC NPs. This can be attributed to the smaller particle size of diPTX NPs (117.20 ± 4.25 nm) and diPC NPs (123.07 ± 2.81 nm) compared to Cel NPs (141.37 ± 3.81 nm), and a smaller size is a key determinant for the prolonged blood circulation time.

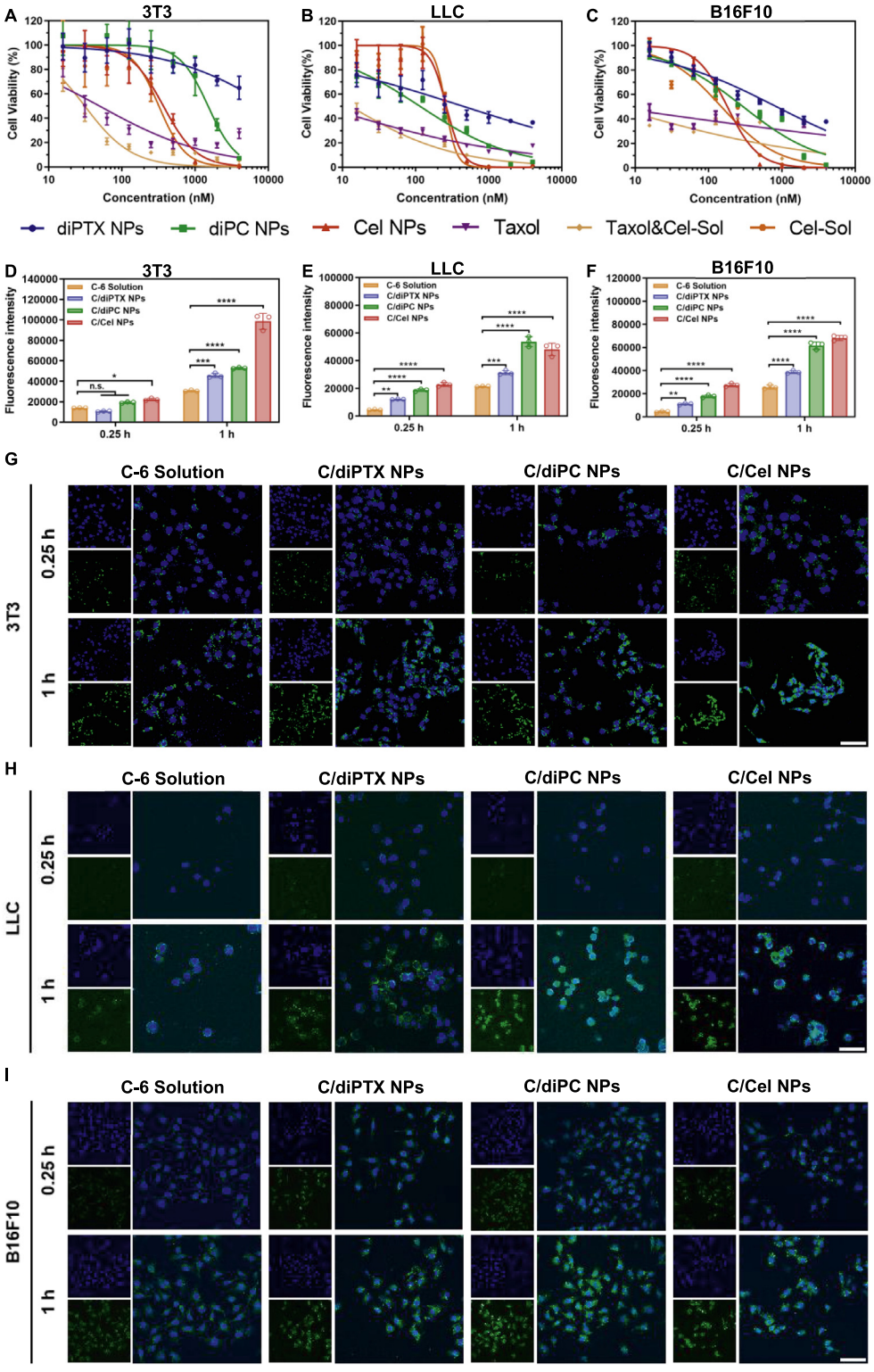


Fig. 2 – Cytotoxicity and cellular uptake of reduction-responsive nanoprodrugs. (A–C) Cytotoxicity of diPTX NPs, diPC NPs, Cel NPs, Taxol, Taxol&Cel-Sol and Cel-Sol against (A) 3T3, (B) LLC) and (C) B16F10 cells after 48 h treatment, as determined using the CCK-8 assay ($n = 6$). (D–F) Quantitative analysis of fluorescence intensity using FCM after 0.25 h and 1 h incubation with C-6 solution, C/diPTX NPs, C/diPC NPs and C/Cel NPs in (D) 3T3, (E) LLC and (F) B16F10 cells. (G–I) CLSM images of (G) 3T3, (H) LLC and (I) B16F10 cells after 0.25- and 1-h incubation with C-6 solution, C/diPTX NPs, C/diPC NPs and C/Cel NPs (scale bar, 100 μm). Data are presented as means ± SD ($n = 3$). Statistical significance: *$P < 0.05$, **$P < 0.01$, ***$P < 0.001$, ****$P < 0.0001$; ns, not significant.

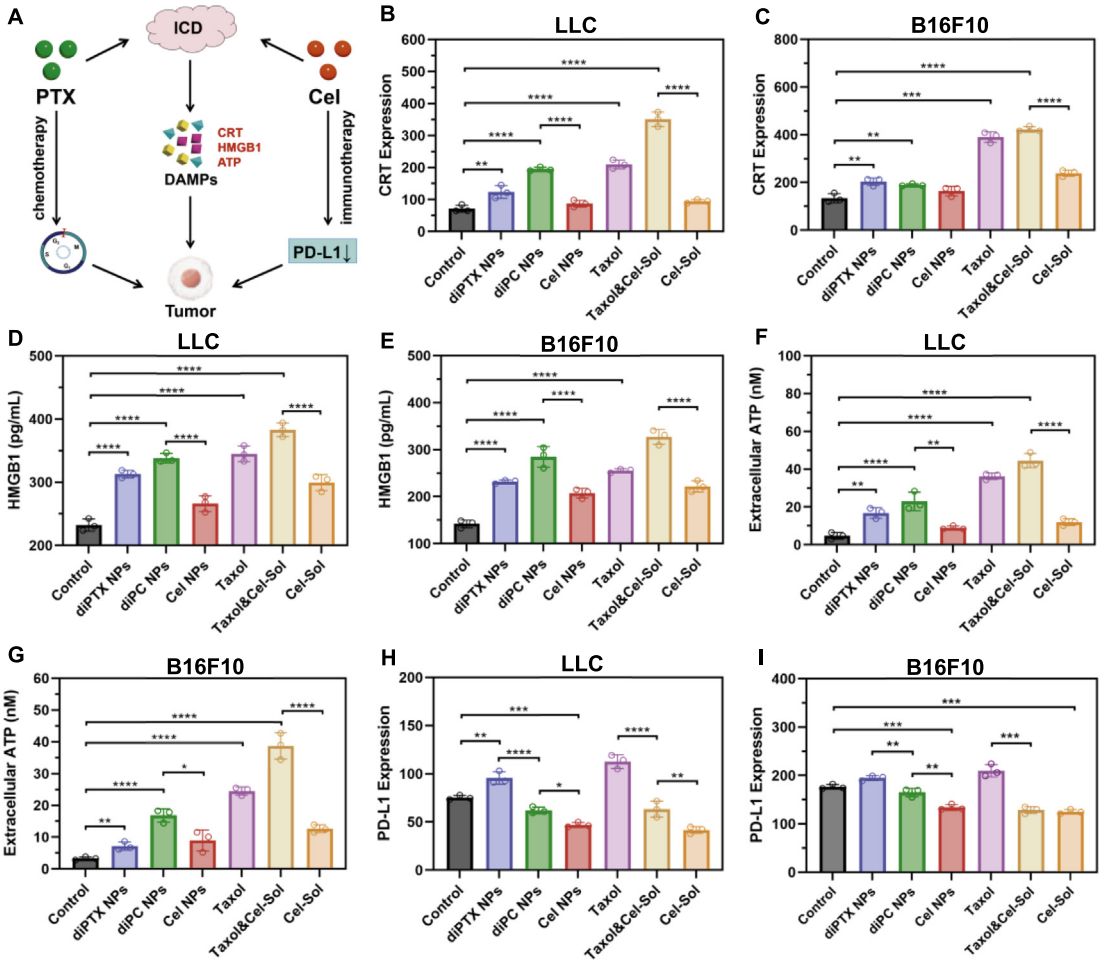


Fig. 3 – Reduction-responsive dimeric nanoprodrugs activate ICD and downregulate PD-L1. (A) Schematic illustration of ICD activation and PD-L1 downregulation. (B–C) CRT exposure in (B) LLC and (C) B16F10 cells after 12-h treatment with diPTX NPs, diPC NPs, Cel NPs, Taxol, Taxol&Cel-Sol, or Cel-Sol (equivalent Cel concentration, 1500 nM), as measured using FCM. (D–G) Quantification of HMGB1 release in (D) LLC and (E) B16F10 cells and ATP efflux in (F) LLC and (G) B16F10 cells, using commercial assay kits. (H–I) PD-L1 expression levels in (H) LLC and (I) B16F10 cells using FCM. Data are presented as means ± SD ($n = 3$). Statistical significance: *$P < 0.05$, **$P < 0.01$, ***$P < 0.001$, ****$P < 0.0001$.

Furthermore, the presence of thiol-containing compounds in the bloodstream, such as GSH and sulfhydryl proteins like albumin, might potentially affect the stability and integrity of Cel NPs as well.

Subsequently, to evaluate the tissue distribution of the NPs, we performed both *in vivo* and *ex vivo* fluorescence imaging in LLC tumor-bearing mice using DiR-labelled NPs. Both imaging modalities showed significantly higher fluorescence intensity for all three NPs compared with the free DiR solution (Fig. 4A). Over time, the NP groups showed increased fluorescence intensity at 24 h compared with 4 h, with quantitative analysis revealing an approximately fourfold higher tumor accumulation at the later time point, demonstrating a clear time-dependent accumulation pattern (Fig. 4B–4C). Notably, organ distribution profiles differed between formulations; the free DiR solution localized predominantly in the lungs, whereas NPs primarily accumulated in the liver. Consistent trends were observed in B16F10 tumor-bearing mice, although the fluorescence intensity in B16F10 tumor tissues was notably lower than that in LLC tumors at equivalent time points. This discrepancy was likely attributable to interference from melanin in B16F10 tumors (Fig. 4D–4F). These findings confirm that diPC NPs effectively accumulate in tumor tissues through a passive targeting mechanism, facilitated by their prolonged circulation time, thereby establishing a foundation for chemoimmunotherapy applications.

3.5. *In vivo antitumor efficacy and biosafety evaluation in LLC models*

Encouraged by the promising antitumor efficacy observed *in vitro*, we established a C57BL/6J mouse model bearing LLC tumors to further evaluate the therapeutic outcomes *in vivo*. Following the experimental scheme outlined in Fig. 5A, when the tumor volume reached 100 mm^3, the mice were randomly allocated into seven groups: saline, diPTX NPs, diPC NPs, Cel NPs, Taxol, Taxol&Cel-Sol, and Cel-Sol. The equivalent intravenous doses were PTX at 10 mg/kg and Cel at

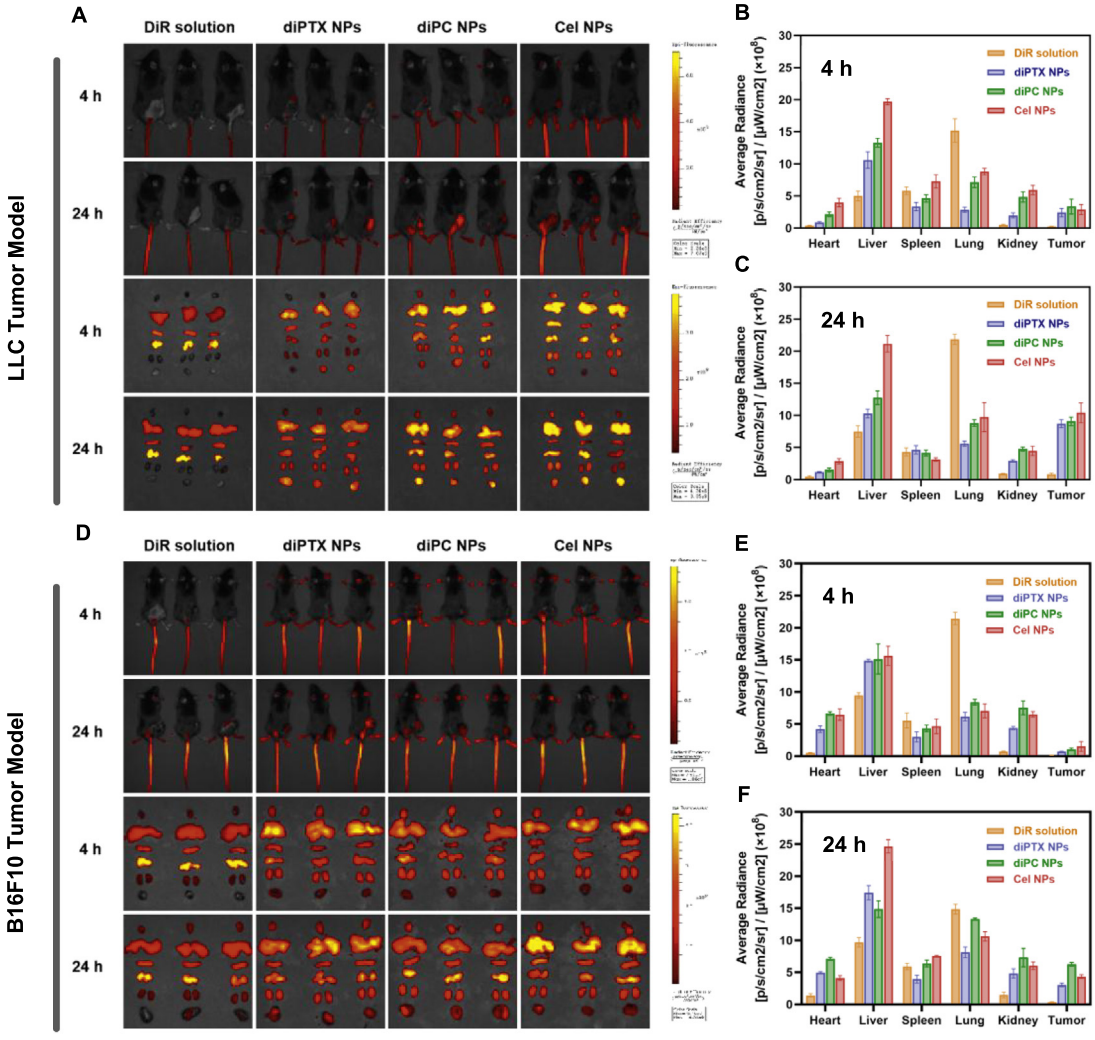


Fig. 4 – Tissue distribution of reduction-responsive dimeric nanoprodrugs. (A) *In vivo* and *ex vivo* fluorescence images of LLC tumor-bearing mice and major organs (arranged from top to bottom: heart, liver, spleen, lungs, kidneys and tumor) at 4 h and 24 h post-injection of DiR solution, diPTX NPs, diPC NPs or Cel NPs. Semiquantitative evaluation of NIR signal intensity in tumor and major organs ($n = 3$). (D) Corresponding *in vivo* and *ex vivo* NIR fluorescence images in B16F10 tumor-bearing models at the same time points. Semiquantitative evaluation of fluorescence accumulation in tumors and organs at (E) 4 h and (F) 24 h after treatment ($n = 3$).

2 mg/kg. Body weight monitoring during treatment revealed mild weight loss in the solution-based treatment groups (Taxol, Taxol&Cel-Sol and Cel-Sol), whereas mice receiving NP formulations maintained stable body weights (Fig. 5B). Tumor growth analysis demonstrated rapid progression in the saline control group, whereas all treatment groups exhibited significant tumor suppression. Notably, diPC NPs displayed the strongest antitumor effect, inhibiting tumor growth by 76% compared with the saline group (Fig. 5C). Consistent with this, tumor size and weight measurements further confirmed the superior efficacy of diPC NPs, with this group showing the smallest tumors (Fig. 5D–5E). To further evaluate the *in vivo* antitumor efficacy of diPC NPs, we performed a histopathological analysis of the tumor tissues. H&E staining images showed that the diPC NPs group exhibited the poorest cellular integrity and the most extensive nuclear ablation. Ki67 staining revealed fewer positive cells in the diPC NPs group, indicating the lowest cellular proliferative activity. TUNEL fluorescence staining revealed markedly enhanced signal intensity in diPC NPs-treated tumors, indicating extensive cellular apoptosis and necrosis (Fig. 5F). Collectively, these histopathological analyses provide compelling evidence that diPC NPs exhibit superior antitumor efficacy compared with all other tested formulations.

Notably, *in vitro* cytotoxicity assays revealed a higher IC_{50} for the diPC NPs group compared with the Taxol group. However, *in vivo* antitumor efficacy results demonstrated that diPC NPs exhibited superior antitumor activity, primarily attributable to their long-circulating properties *in vivo*, reduction-responsive release mechanism, and immune-activating effects. The PEG hydration layer of diPC NPs prolonged their systemic circulation time, facilitating passive accumulation in tumor tissue *via* the EPR effect, whereas Taxol lacked passive tumor accumulation capability. Additionally,

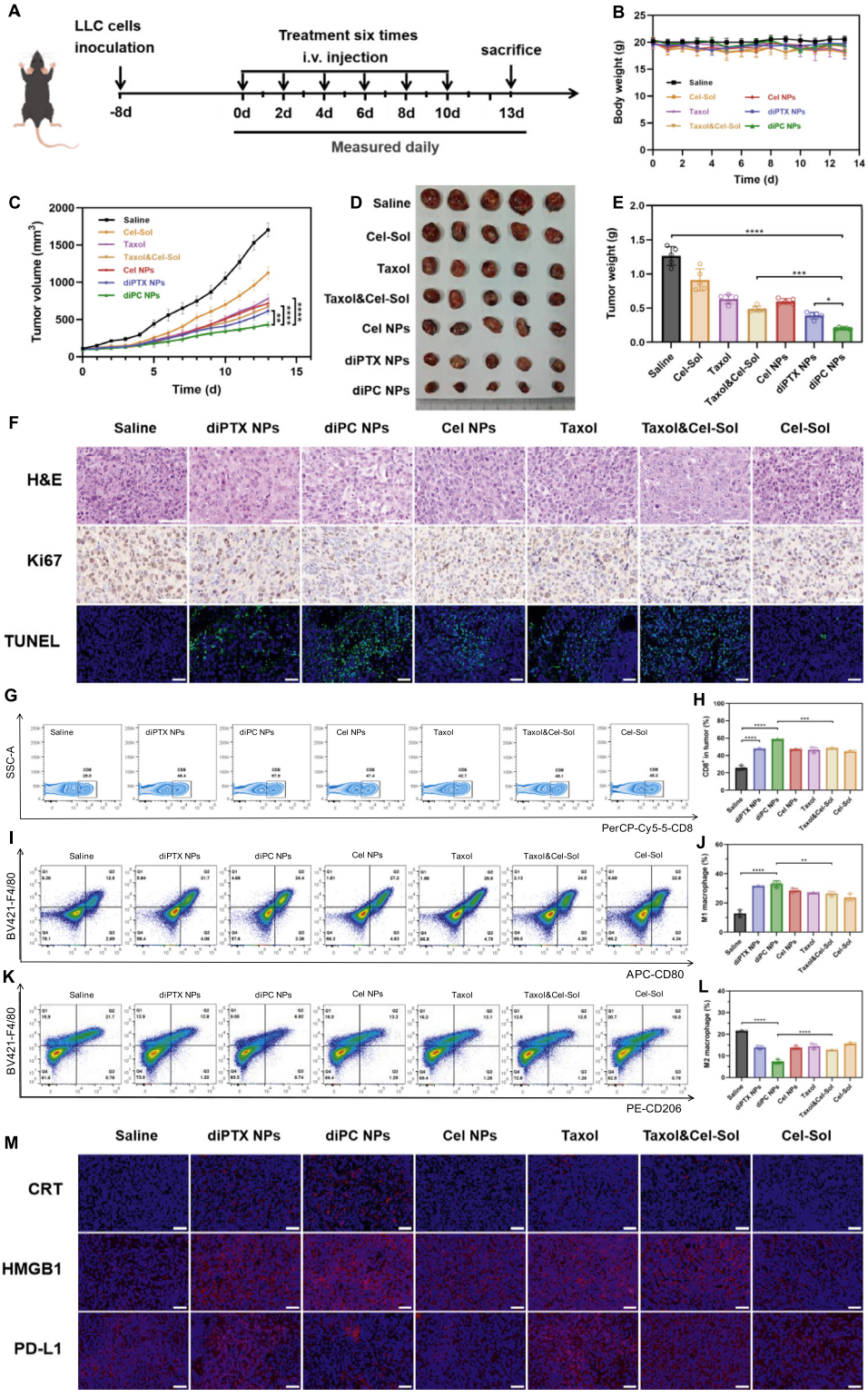


Fig. 5 – *In vivo* antitumor efficacy and biosafety of reduction-responsive dimeric nano prodrugs in LLC tumor-bearing mice. (A) Experimental protocol for LLC tumor-bearing mice. (B) Changes in mouse body weight during treatment. (C) Tumor growth curves. (D) Photographs of excised tumors. (E) Weights of excised tumors. (F) H&E, Ki67 and TUNEL staining images of tumor tissues (Scale bar: 50 μm). FCM analysis of lymphocyte infiltration: (G) FCM plots, (H) quantitative results. FCM analysis of macrophage subsets: (I) M1 macrophage levels, (J) quantitative results for M1 macrophages, (K) M2 macrophage levels, (L) quantitative results for M2 macrophages. (M) Immunofluorescence analysis of CRT exposure, HMGB1 secretion and PD-L1 expression in tumors Scale bar: 100 μm). Data are presented as means ± SD ($n = 5$). Statistical significance: *$P < 0.05$, **$P < 0.01$, ***$P < 0.001$, ****$P < 0.0001$.

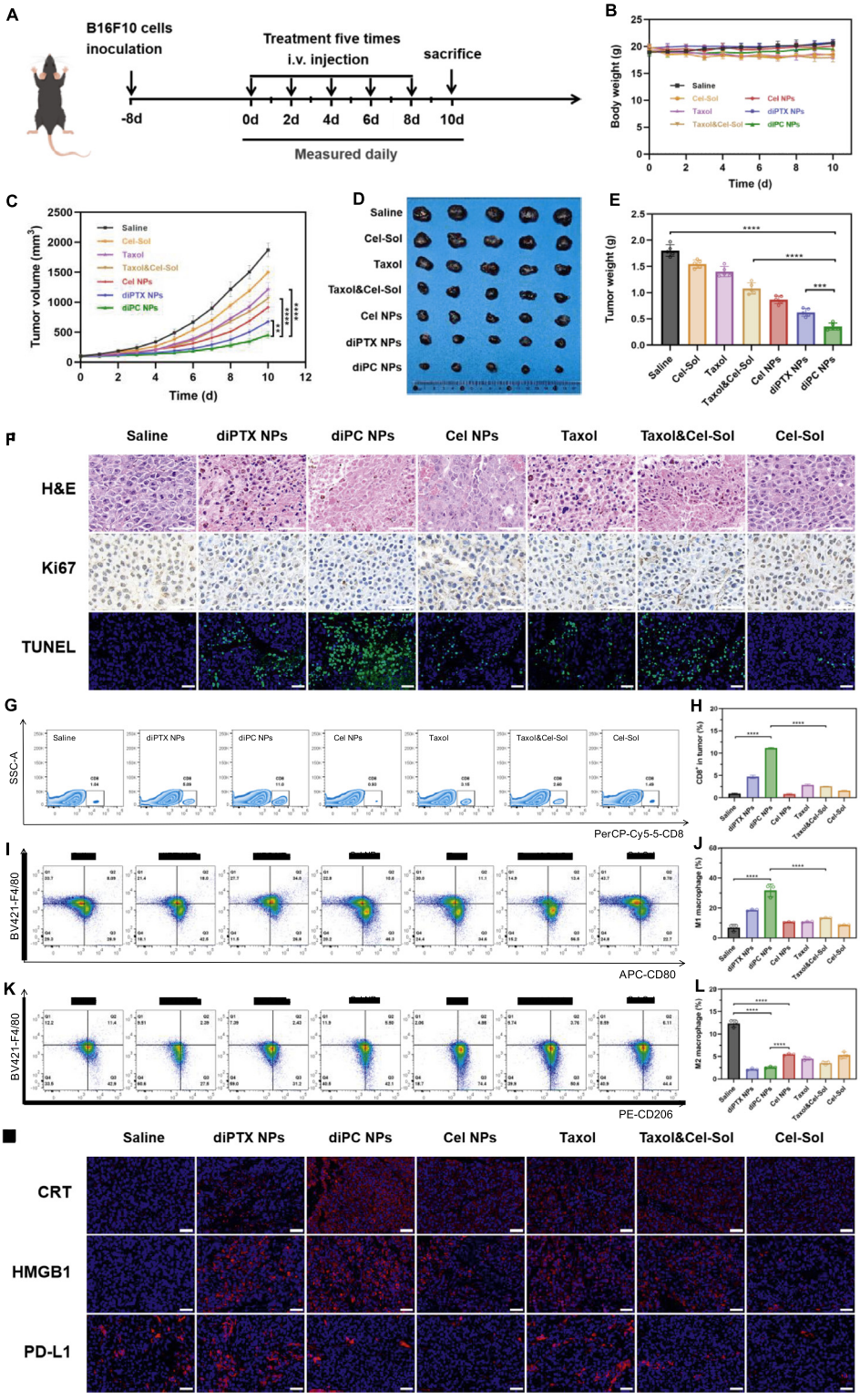


Fig. 6 – *In vivo* antitumor efficacy and biosafety of reduction-responsive dimeric nanoprodrugs in B16F10 tumor-bearing mice. (A) Experimental protocol for B16F10 tumor-bearing mice. (B) Changes in mouse body weight during treatment. (C) Tumor growth curves. (D) Photographs of excised tumors. (E) Weights of excised tumors. (F) H&E, Ki67 and TUNEL staining images of tumors (Scale bar: 50 μm). FCM analysis of lymphocyte infiltration: (G) Representative FCM plots, (H) quantitative results. FCM analysis of macrophage subsets: (I) M1 macrophage levels, (J) quantitative results for M1 macrophages, (K) M2 macrophage levels, (L) quantitative results for M2 macrophages. (M) Immunofluorescence analysis of CRT exposure, HMGB1 secretion, and PD-L1 expression in tumors (Scale bar: 50 μm). Data are presented as means ± SD ($n = 5$). Statistical significance: $^{**}P < 0.01$, $^{***}P < 0.001$, $^{****}P < 0.0001$.

diPC NPs possessed reduction-responsive characteristics, enabling sustained drug release in the TME with high GSH levels, thereby maintaining prolonged drug exposure at the tumor site—the release of PTX from nanoprodrug might decay the rate of PTX-mediated chemotherapy. Most importantly, the Cel contained within diPC NPs downregulates PD-L1, modulating the immunosuppressive TME through immune checkpoint blockade. This immunotherapeutic effect could not be adequately assessed by conventional *in vitro* toxicity assays.

To evaluate the biosafety profile of diPC NPs, we performed comprehensive histological and hematological analyses. H&E staining of major organs revealed well-preserved tissue architecture without pathological abnormalities in all treatment groups (Fig. S12). Comparative analysis revealed that mice treated with diPC NPs maintained normal hematological profiles, with all measured parameters showing no statistically significant differences from saline controls. This finding confirms the absence of systemic inflammation or hematological toxicity. Hepatic and renal function biomarkers were similarly unaffected, with values remaining within normal physiological ranges (Fig. S13). These results collectively demonstrate that diPC NPs exhibit excellent *in vivo* biosafety.

To elucidate the immunomodulatory effects of diPC NPs, we performed comprehensive immune profiling of TMEs in LLC-bearing C57BL/6J mice using FCM. The results demonstrated that the diPC NPs group exhibited the highest proportion of tumor-infiltrating $CD8^+$ T cells, which was 1.3-fold higher than that in the saline control group (Fig. 5G–5H). Furthermore, immunophenotyping demonstrated a marked shift in macrophage polarization, and treatment with diPC NPs led to an increase in M1 macrophage infiltration accompanied by a decrease in M2 macrophages (Fig. 5I–5L). This profound reprogramming of the tumor immune microenvironment from an immunosuppressive (M2-dominant) to an immunostimulatory (M1-dominant) phenotype underscores the potent immunomodulatory and antitumor efficacy of diPC NPs. Immunofluorescence staining of CRT, HMGB1, and PD-L1 was performed on tumor tissues across different groups. The results revealed that the diPC NPs group demonstrated pronounced CRT exposure and HMGB1 release, suggesting potent ICD induction in tumors, thereby driving immune microenvironment remodeling. Notably, diPC NPs simultaneously suppressed the immune checkpoint molecule PD-L1, effectively disrupting tumor immune evasion mechanisms while enhancing ICD signals (Fig. 5M). Western blotting (WB) analysis further confirmed that diPC NPs downregulated PD-L1 expression compared with the diPTX NPs and Taxol groups (Fig. S14). These results collectively demonstrate that diPC NPs activate robust antitumor immune responses *in vivo* through potent ICD induction while simultaneously improving the immunosuppressive TME by PD-L1 downregulation.

3.6. *In vivo antitumor efficacy and biosafety evaluation in B16F10 models*

Additionally, we established B16F10 bearing C57BL/6J mice model, and the experiment was conducted according to Fig. 6A. Consistent with previous observations, the body weight of the nanoparticle-treated group did not significantly change (Fig. 6B), indicating good biocompatibility. Tumors in the saline group grew rapidly, whereas all treatment groups exhibited varying degrees of antitumor activity, with the diPC NPs group showing the most delayed tumor volume growth (Fig. 6C). Images of excised tumors and tumor weights further verified that the diPC NPs group had the optimal tumor suppression capability (Fig. 6D–6E). H&E staining images revealed severely disrupted cellular architecture and extensive nuclear fragmentation in the diPC NPs group, indicative of substantial tumor damage. Furthermore, Ki67 and TUNEL staining demonstrated significantly reduced tumor cell proliferation and the highest degree of apoptosis in the diPC NPs-treated tumors (Fig. 6F). Importantly, H&E staining revealed no apparent pathological changes or tissue injury in the principal organs of any treatment group. (Fig. S15). Furthermore, comprehensive hematological and biochemical analyses showed no significant deviations in CBCs or hepatic/renal function parameters (Fig. S16), further validating the outstanding biosafety profile of the diPC NPs.

Subsequently, we used FCM to analyze changes in the immune microenvironment within tumor cells across all treatment groups. Compared with other treatment groups, diPC NPs treatment significantly enhanced $CD8^+$ T-cell infiltration in tumors (Fig. 6G–6H). Furthermore, diPC NPs treatment resulted in a higher proportion of M1-type macrophages and fewer M2-type macrophages in tumor tissues, further demonstrating their superior antitumor immune response *in vivo* (Fig. 6I–6L). Meanwhile, the antitumor immune response was evaluated through immunofluorescence staining of CRT, HMGB1, and PD-L1 in tumor tissues. As shown in Fig. 6M, tumor tissues in the diPC NPs group exhibited significant CRT exposure and HMGB1 release. More importantly, although both diPTX NPs and Taxol groups showed marked upregulation of PD-L1 that promoted immune escape, this effect was reversed by diPC NP treatment. WB analysis revealed that diPC NPs significantly reduced PD-L1 expression compared with diPTX NPs and Taxol groups, which was consistent with the immunofluorescence findings (Fig. S17). These comprehensive results demonstrate that diPC NPs not only activate potent antitumor immunity but also effectively remodel the immunosuppressive TME through multiple mechanisms.

4. Conclusions

In summary, we report a carrier-free, reduction-responsive nanoprodrug (diPC NPs) formed by the co-assembly of a PTX dimer prodrug and Cel for synergistic tumor chemoimmunotherapy. The diPC NPs exhibited excellent stability, favorable reduction responsiveness, prolonged blood circulation, and enhanced tumor accumulation. Once internalized into tumor cells, the disulphide bonds were cleaved by endogenous GSH, resulting in the rapid release of PTX and Cel. The released PTX and Cel promoted tumor cell apoptosis, induced a robust ICD response, and significantly suppressed tumor growth in LLC and

B16F10 tumor-grafted mice, in combination with Cel-triggered PD-L1 downregulation. Our work highlights a promising strategy through the precise integration of a chemotherapeutic agent and an immunomodulator for combinational chemoimmunotherapy.

Conflicts of interest

The authors declare that there is no conflicts of interest.

CRediT authorship contribution statement

Yudi Lu: Writing – original draft, Visualization, Methodology, Data curation. **Mei Zhou:** Supervision, Software, Investigation, Formal analysis. **Xunfa Zhang:** Validation, Resources, Investigation, Data curation. **Weijun Huang:** Supervision, Software, Resources. **Fan Li:** Visualization, Validation, Investigation. **Ning Li Zhang:** Supervision, Methodology, Formal analysis. **Nannan Lu:** Writing – review & editing, Supervision, Funding acquisition, Formal analysis. **Chenggui Wu:** Writing – review & editing, Investigation, Conceptualization. **Zhihui Feng:** Writing – review & editing, Methodology, Investigation, Funding acquisition, Formal analysis, Conceptualization. **Shuangying Gui:** Writing – review & editing, Supervision, Resources, Formal analysis, Conceptualization. **Zhenbao Li:** Writing – review & editing, Supervision, Resources, Project administration, Funding acquisition.

Acknowledgments

The authors acknowledge financial support from the National Natural Science Foundation of China (No. 82374301), the State Key Laboratory of Southwestern Chinese Medicine Resources (No. SKLTCM202410), the Key Project of Anhui Province Department of Education (No. 2023AH030070, 2024AH051040), Anhui Province Key Laboratory, China (KFKT202305, KFKT202507, 2024ZYFBAHKLA11, and 2024ZYFBAHKLA15), and Greater Health Research Institute of Hefei Comprehensive National Science Center, China (2023CXMMTCM005).

Supplementary materials

Supplementary material associated with this article can be found, in the online version, at doi:10.1016/j.ajps.2026.101124. The figures and tables with "S" before the serial number are included in the Supplementary data.

References

[1] Bray F, Laversanne M, Sung H, Ferlay J, Siegel RL, Soerjomataram I, et al. Global cancer statistics 2022: GLOBOCAN estimates of incidence and mortality worldwide for 36 cancers in 185 countries. CA Cancer J Clin 2024;74(3):229–63.

[2] Labrie M, Brugge JS, Mills GB, Zervantonakis IK. Therapy resistance: opportunities created by adaptive responses to targeted therapies in cancer. Nat Rev Cancer 2022;22(6):323–39.

[3] Letai A, de The H. Conventional chemotherapy: millions of cures, unresolved therapeutic index. Nat Rev Cancer 2025;25(3):209–18.

[4] Sun L, Zuo C, Ma B, Liu X, Guo Y, Wang X, et al. Intratumoral injection of two dosage forms of paclitaxel nanoparticles combined with photothermal therapy for breast cancer. Chin Herb Med 2025;17(1):156–65.

[5] Wang TH, Wang HS, Soong YK. Paclitaxel-induced cell death: where the cell cycle and apoptosis come together. Cancer 2000;88(11):2619–28.

[6] Xie S, Ogden A, Aneja R, Zhou J. Microtubule-binding proteins as promising biomarkers of paclitaxel sensitivity in cancer chemotherapy. Med Res Rev 2016;36(3):300–12.

[7] Zhang B, Zhou S, Lu S, Xiang X, Yao X, Lei W, et al. Paclitaxel prodrug enables glutathione depletion to boost cancer treatment. ACS Nano 2024;18(40):26690–703.

[8] Galluzzi L, Guilbaud E, Schmidt D, Kroemer G, Marincola FM. Targeting immunogenic cell stress and death for cancer therapy. Nat Rev Drug Discov 2024;23(6):445–60.

[9] Serpico AF, Pisauro C, Grieco D. cGAS-dependent proinflammatory and immune homeostatic effects of the microtubule-targeting agent paclitaxel. Front Immunol 2023;14:1127623.

[10] Hu N, Xue H, Zhang T, Fan Y, Guo F, Li Z, et al. Harnessing PD-1 cell membrane-coated paclitaxel dimer nanoparticles for potentiated chemoimmunotherapy. Biomed Pharmacother 2024;174:116482.

[11] Yi M, Zheng X, Niu M, Zhu S, Ge H, Wu K. Combination strategies with PD-1/PD-L1 blockade: current advances and future directions. Mol Cancer 2022;21(1):28.

[12] Melero I, de Miguel Luken M, de Velasco G, Garralda E, Martín-Liberal J, Joerger M, et al. Neutralizing GDF-15 can overcome anti-PD-1 and anti-PD-L1 resistance in solid tumours. Nature 2025;637(8031):1218–27.

[13] Nielsen DL, Juhl CB, Nielsen OH, Chen IM, Herrmann J. Immune checkpoint inhibitor-induced cardiotoxicity: a systematic review and meta-analysis. JAMA Oncol 2024;10(10):1390–9.

[14] Yue Y, Su L, Wang Y, Li X, Xiao X, Xie J, et al. Banxia Xiexin decoction inhibits colitis-associated colorectal cancer development by modulating STAT3 signaling and gut microbiota. Chin Herb Med 2025;17(3):380–91.

[15] Qian X, Liu Y, Chen W, Zheng S, Lu Y, Qiu P, et al. Paris saponin VII induces caspase-3/GSDME-dependent pyroptosis in pancreatic ductal adenocarcinoma cells by activating ROS/bax signaling. Chin Herb Med 2025;17(1):94–107.

[16] Wang CY, Bai XY, Wang CH. Traditional Chinese medicine: a treasured natural resource of anticancer drug research and development. Am J Chin Med 2014;42(3):543–59.

[17] Wang C, Dai S, Zhao X, Zhang Y, Gong L, Fu K, et al. Celastrol as an emerging anticancer agent: current status, challenges and therapeutic strategies. Biomed Pharmacother 2023;163:114882.

[18] Qiu N, Liu Y, Liu Q, Chen Y, Shen L, Hu M, et al. Celastrol nanoemulsion induces immunogenicity and downregulates PD-L1 to boost abscopal effect in melanoma therapy. Biomaterials 2021;269:120604.

[19] Li HF, Zhu N, Wu JJ, Shi YN, Gu J, Qin L. Celastrol elicits antitumor effects through inducing immunogenic cell death and downregulating PD-L1 in ccRCC. Curr Pharm Des 2024;30(15):1265–78.

[20] Ji Y, Hao J, Tao X, Li Z, Chen L, Qu N. Preparation and anti-tumor activity of paclitaxel silk protein nanoparticles encapsulated by biofilm. Pharm Dev Technol 2024;29(5):627–38.

[21] Zhang X, Chen Y, Li X, Xu H, Yang J, Wang C, et al. Carrier-free self-assembled nanomedicine based on celastrol and galactose for targeting therapy of hepatocellular carcinoma via inducing ferroptosis. Eur J Med Chem 2024;267:116183.
[22] Subbaiah MAM, Rautio J, Meanwell NA. Prodrugs as empowering tools in drug discovery and development: recent strategic applications of drug delivery solutions to mitigate challenges associated with lead compounds and drug candidates. Chem Soc Rev 2024;53(6):2099–210.
[23] Ciftci F, Özarslan AC, İmran CK, Yelkenci A, Tavukcuoglu O, Ghorbanpour M. Advances in drug targeting, drug delivery, and nanotechnology applications: therapeutic significance in cancer treatment. Pharmaceutics 2025;17(1):121.
[24] Li G, Sun B, Li Y, Luo C, He Z, Sun J. Small-molecule prodrug nanoassemblies: an emerging nanoplatform for anticancer drug delivery. Small 2021;17(18):e2101460.
[25] Li Y, Sun Y, Yan Q, Wang W, Wang S, Wang Q, et al. Redox-triggered prodrug nanoassemblies with high tumor selectivity and biocompatibility break through antitumor dilemma of paclitaxel. Chinese Chem Lett 2025:111350.
[26] Zhang Y, Zhang W, Wang Y, Zhu J, Zhou M, Peng C, et al. Emerging nanotaxanes for cancer therapy. Biomaterials 2021;272:120790.
[27] Luo C, Sun B, Wang C, Zhang X, Chen Y, Chen Q, et al. Self-facilitated ROS-responsive nanoassembly of heterotypic dimer for synergistic chemo-photodynamic therapy. J Control Release 2019;302:79–89.
[28] Li F, Wang W, Xu W, Li W, Lu Y, Wang R, et al. Traditional Chinese medicine-facilitated redox-labile paclitaxel dimer nanoprodrug for efficient chemoimmunotherapy. J Pharm Anal 2025:101348.
[29] Sun B, Luo C, Zhang X, Guo M, Sun M, Yu H, et al. Probing the impact of sulfur/selenium/carbon linkages on prodrug nanoassemblies for cancer therapy. Nat Commun 2019;10(1):3211.
[30] Liu T, Li L, Wang S, Dong F, Zuo S, Song J, et al. Hybrid chalcogen bonds in prodrug nanoassemblies provides dual redox-responsivity in the tumor microenvironment. Nat Commun 2022;13(1):7228.
[31] Zhang H, Liu T, Sun Y, Wang S, Wang W, Kuang Z, et al. Carbon-spaced tandem-disulfide bond bridge design addresses limitations of homodimer prodrug nanoassemblies: enhancing both stability and activatability. J Am Chem Soc 2024;146(32):22675–88.
[32] Pei Q, Hu X, Liu S, Li Y, Xie Z, Jing X. Paclitaxel dimers assembling nanomedicines for treatment of cervix carcinoma. J Control Release 2017;254:23–33.
[33] Qian X, Yang H, Ye Z, Gao B, Qian Z, Ding Y, et al. Celecoxib augments paclitaxel-induced immunogenic cell death in triple-negative breast cancer. ACS Nano 2024;18(22):15864–77.
[34] Yang Y, Liu X, Zhang R, Liu Y, Zhou N, Jiang Y. Size-tunable micro-nano liposomes: enhanced lung targeting and tumor penetration for combination treatment of lung cancer. Small 2025;21(2):e2409593.
[35] Li L, Wang H, Zhang S, Gao S, Lu X, Pan Y, et al. Statins inhibit paclitaxel-induced PD-L1 expression and increase $CD8^+$ T cytotoxicity for better prognosis in breast cancer. Int J Surg 2024;110:4716–26.
[36] Geng Y, Xiang J, Shao S, Tang J, Shen Y. Mitochondria-targeted polymer-celastrol conjugate with enhanced anticancer efficacy. J Control Release 2022;342:122–33.